Coexistence of charge density wave and field-tuned magnetic states in $TmNiC_2$

Kamil K. Kolincio[1,*] Marta Roman[2,3] Valerio Tammurello,[4] Simone Di Cataldo,[4] Daniel Matulka[5] Sonia Francoual[6] Berthold Stöger[5] and Herwig Michor[2]

[1]*Faculty of Applied Physics and Mathematics, Gdańsk University of Technology, Narutowicza 11/12, 80-233 Gdańsk, Poland*
[2]*Institute of Solid State Physics, TU Wien, Wiedner Hauptstrasse 8–10, A-1040 Wien, Austria*
[3]*Institute of Physics and Applied Computer Science, Faculty of Applied Physics and Mathematics, Gdańsk University of Technology, Narutowicza 11/12, 80-233 Gdańsk, Poland*
[4]*Dipartimento di Fisica, Sapienza University of Rome, Piazzale Aldo Moro 5, 00185 Rome, Italy*
[5]*X-Ray Center, TU Wien, Getreidemarkt 9, A-1060 Wien, Austria*
[6]*Deutsches Elektronen-Synchrotron DESY, 22607 Hamburg, Germany*

(Received 9 May 2024; revised 15 April 2025; accepted 14 May 2025; published 5 June 2025)

Exploring the relations between coexisting, cooperative, or competing types of ordering is a key to identify and harness the mechanisms governing the mutual interactions between them and to utilize their combined properties. We have experimentally explored the response of the charge density wave (CDW) to various antiferromagnetic, metamagnetic, and field-aligned ferromagnetic states that constitute the magnetic phase diagram of $TmNiC_2$. The high-resolution x-ray diffraction experiment employing synchrotron radiation at low temperature and high magnetic field allowed one to follow the superstructure satellite reflections, being a sensitive probe of CDW. This investigation not only reveals direct evidence that the charge density wave avoids even a partial suppression in the antiferromagnetic ground state, but also proves that this state coexists, without any visible signatures of weakening, in the entire dome of the magnetically ordered phases, including the field-aligned ferromagnetic state. The calculations of the electronic and phonon structures support the experiment, revealing that the dominant contribution to the CDW transition stems from momentum-dependent electron-phonon coupling. We conclude that this mechanism prevents the CDW from vanishing, although the nesting conditions within the magnetically ordered phases deteriorate.

DOI: 10.1103/PhysRevB.111.245116

I. INTRODUCTION

The interactions between the various charge and magnetic degrees of freedom are the object of an extensive investigation aimed to understand and control the related macroscopic observables [1–6]. A particularly close relationship can exist between entities that are based on the same foundation, e.g., the electronic structure. An example of the latter is charge density wave (CDW) order and magnetism driven by the Ruderman-Kittel-Kasuya-Yosida (RKKY) mechanism [7–9]. CDW, seen in quasi-low-dimensional materials, is predicted by the canonical Peierls-Fröhlich model [10,11] to originate from the nesting of parallel segments of the Fermi surface (FS) assisted by coupling between electrons and phonons and accompanied by crystal structure modulation. RKKY magnetism of rare-earth-based metals, leading even to the formation of topologically nontrivial spin textures such as magnetic skyrmions [12], relies on itinerant electrons which mediate the interaction between local magnetic moments, and thus is sensitive to charge distribution in space and to the Fermi surface contour [13]. The relation between CDW and magnetism can show either a constructive or destructive character. On the one hand, the presence of a readily developed charge modulation may serve as a template for spin fluctuations and eventually govern the onset of a magnetically ordered state [14]. On the other hand, long-range magnetic ordering, particularly ferromagnetism, competes with the charge density wave state [15–17]. Therefore, the number of systems in which both entities coexist is severely limited.

One of the systems in which both types of ordering occur is the $RNiC_2$ family, where R stands for a rare-earth ion. Within this group of compounds, at least two kinds of CDWs have been reported. The formation of Ni-Ni pairs entails structural modulation with modulation wave vectors, $q_1 = (0.5, 0.5 + \eta, 0)$, characteristic for early-lanthanide-based family members [18–20], and commensurate $q_2 = (0.5, 0.5, 0.5)$, dominating the late-lanthanide-based $RNiC_2$ [21]. The q_1-type CDW has been suggested not only to coexist but also to scaffold the antiferromagnetic state (AFM) occurring in $NdNiC_2$ and $GdNiC_2$ with almost identical periodicity (propagation vector) as the CDW lattice modulation [19,22]. The field-induced transitions to metamagnetic (MM) and field-aligned ferromagnetic (FA-FM) states yet entirely suppress this type of CDW [22]; this effect has also been

*Contact author: kamil.kolincio@pg.edu.pl

observed at the onset of the ferromagnetic ground state in $SmNiC_2$ [23,24]. The q_2-type CDW, however, exhibits the signatures of a distinct response to the magnetic ordering. Maeda *et al.* [21] have demonstrated that this state remains entirely untouched upon crossing the Néel temperature and onset of the AFM phase in $DyNiC_2$, $HoNiC_2$, and $ErNiC_2$. Moreover, the arguments raised upon the transport and magnetotransport properties of polycrystalline samples of $TmNiC_2$ [25], $HoNiC_2$, and $ErNiC_2$ [26] suggest that unlike q_1-type CDW, the q_2-type CDW also survives in the MM and FA-FM phases. However, the limitation of the experiments performed on a polycrystalline material is that they provide only an indirect probe of the CDW. While magnetoresistance and Hall responses deliver information on the carrier density and mobility, strongly influenced by CDW via Fermi surface reconstruction, they can also be affected by different, CDW-independent factors such as the presence of Weyl nodes, as predicted to occur in the electronic structure of $RNiC_2$ [27]. Therefore, although the previous studies delivered substantial clues, the direct proof required to unambiguously confirm or deny the robustness of CDW order across the field-induced magnetic states is missing.

Regardless of the mechanism triggering the Peierls transition to a CDW state, and its impact on the electronic structure, the essence of this state is the spatial modulation of electronic charge density, concomitant with the lattice distortion with matching periodicity [28,29]. The related satellite peaks, which are observable by diffraction methods, are thus a sensitive probe of the CDW order parameter. They can be traced under evolving external conditions or across the boundaries of competing or intertwined states [1,30]. In this paper, we present a direct investigation of the CDW response to long-range magnetism by means of the single-crystal x-ray diffraction technique.

II. EXPERIMENTAL AND CALCULATION METHODS

A. Crystal growth and bulk characterization

All experiments were performed on a single-crystalline sample of $TmNiC_2$ grown with the floating zone technique, as previously described in Ref. [31]. Field- and temperature-dependent magnetization measurements were conducted using the vibrating sample magnetometry (VSM) option of a Physical Property Measurement System (PPMS). Low-temperature specific-heat data at zero external magnetic field and at 0.3 T were collected with a homemade calorimeter employing an adiabatic step-heating technique.

B. High-temperature diffraction experiment

To determine the temperature dependence of the amplitude of Ni atom displacements, diffraction data of a small fragment of a $TmNiC_2$ crystal were collected using Mo K_α radiation on a Bruker KAPPA APEX II diffractometer system equipped with an Oxford Cryostream cooling system. A dry stream of nitrogen was used in the 100–300 K range (10 K/step). Frame data of both twin domains were reduced to intensity values using SAINT-PLUS (HKLF 5 file format with reflection overlap information) and a correction for absorption effects was applied using the multiscan approach implemented in TWINABS [32]. The structures were refined using SHELX using a common starting structure. One-hundred refinement cycles resulted in full convergence in all cases.

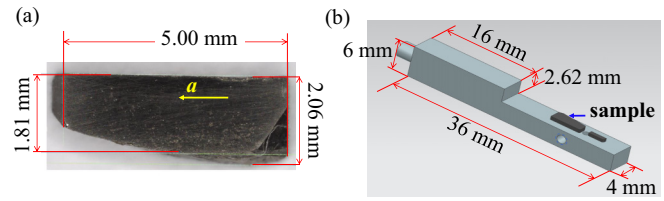

FIG. 1. (a) The $TmNiC_2$ sample used for the diffraction experiment. Dimensions and crystallographic a-axis direction are displayed. Sample thickness, not shown in the figure, is $t = 0.66$ mm. (b) Oxygen-free copper sample holder used for the synchrotron experiment with its key dimensions. The largest surface of the sample, parallel to the (011) plane, contacts the holder to maximize the heat exchange, and to ensure the mechanical stability of the sample exposed to strong magnetic field.

C. Synchrotron diffraction experiment

The low-temperature and high-field diffraction experiment has been performed at the P09 beamline of Petra III synchrotron equipped with a 14 T superconducting cryomagnet [33] and a variable-temperature insert. We have used a horizontal scattering geometry with a Dectris PILATUS 300k pixel detector. In this experimental setup, the $h = 0$ main reflections diffract in the horizontal scattering plane ($\gamma = 0$) [33,34]. By choosing a radiation energy of 25 keV (wavelength $\lambda = 0.49594$ Å), the $h = \pm\frac{1}{2}$ satellites diffract in a vertical out-of-plane angle of $\gamma = \sin^{-1}(\frac{\lambda}{2a}) = 4.07^\circ$ (assuming $a = 3.49$ Å), which is comfortably in the range of the $\pm 5^\circ$ vertical opening of the x-ray window. The selected energy of 25 keV is away from any resonance lines related to the elements in $TmNiC_2$.

Since magnetic ordering onsets at a Néel temperature as low as $T_N = 5.5$ K, it is of crucial importance to ensure stable experimental conditions and to exclude the possibility that beam heating effects increase the temperature to such an extent that T_N is exceeded from below.

To facilitate heat dissipation, we have used a sample holder that is custom-made of highly conducting, oxygen-free copper, and mounted the sample with a thin layer of Loctite Stycast 2850 FT. The sample dimensions—area S and thickness t, with ratio $\frac{S}{t} = 14.37$ mm—were optimized to maximize the heat contact. The picture of the sample and the drawing of the sample holder, which serves as a heat sink, are shown in Fig. 1. At the P09 beamline, at liquid helium temperatures, and x-ray energies of ≈ 8 keV where the photon flux is maximum, an attenuation factor of $R_v = 50$ is usually used to ensure that the sample remains at base temperature where the sample surface is directly cooled by the pumped cold helium gas. However, here, as the AFM order parameter could not be directly probed, in order to guarantee that T_N is not exceeded, 10 to 20 times higher attenuation factors have been used. For the scans at temperatures above 3 K, the beam was attenuated by a factor of $R_v = 500$ when scanning both satellite reflections, while the Bragg peaks (0, 5, 7) and (0, 6,

8) have been measured with an attenuation factor of 5000 and 1000, respectively. The scans at 2.9 K have been conducted with attenuation rate $R_v = 1000$, and 12 333 for satellite, and Bragg peaks, respectively. The total power carried by the beam reaching the sample is 28 μW at $R_v = 500$, and 14 μW when applying a higher attenuation factor $R_v = 1000$ [see the Supplemental Material (SM) [35] for further details]. To estimate the maximum temperature increase ΔT at the illuminated sample spot, we have considered a worst-case scenario, entirely neglecting the convection cooling mechanism and relying solely on the conduction channel. We have compared the sample geometry and thermal conductivity at relevant temperatures with the reference experiment performed previously on a $TmVO_4$ sample [34], which, while illuminated by 26 μW of incident beam, was stably maintained at 1.9 K under high vacuum, and thus was cooled by the conduction mechanism alone. We find that even with the most cautious approach case, ΔT is lower than 0.3 K and the sample temperature remains far below T_N (see the SM [35] for more details).

We emphasize that our worst-case estimate does not take into account the presence of exchange gas (He) in the sample chamber, which directly cools down the radiation-exposed sample surface, and thus more effectively minimizes the beam heating effects than heat conduction through sample and sample holder. Moreover, our model does not capture the fraction of photons which are diffracted—not absorbed—and thus do not contribute to the heat process. We then conclude that the real heating effect is significantly weaker than estimated here, and the parameters chosen by us are more than sufficient to rule out any relevant beam heating effects [34].

D. DFT calculations

To compute the electronic structure and phonon dispersion, we employed density functional theory (DFT) and density functional perturbation theory (DFPT) calculations, as implemented in QUANTUM ESPRESSO [36,37]. Phonon linewidths were computed from the imaginary part of the phonon self-energy, with Wannier-interpolated electron-phonon matrix elements, as implemented in EPW [38–40]. The nesting function was computed in the constant-matrix approximation, as defined in Ref. [39]. DFT calculations were performed using optimized norm-conserving Vanderbilt pseudopotentials [41], employed with a Perdew-Burke-Ernzerhof (PBE) exchange-correlation functional [42], within the frozen-core approximation. For the self-consistent calculation of the ground-state charge density, we expanded the Kohn-Sham wave functions in plane waves, with a cutoff of 120 Ry, and integrated over a $10 \times 10 \times 10$ grid in the Brillouin zone, with a 0.005 Ry smearing on the electronic occupations. Phonon calculations were performed on a $4 \times 4 \times 4$ grid of wave vectors. A satisfying Wannierization of the bands close to the Fermi energy is obtained including eight Wannier functions, with an energy window up to 5.2 eV (relative to the Fermi energy), a frozen energy window from −0.2 to 1.9, and an initial guess with $5d$ orbitals over Ni, and three sp^2-like orbitals in the middle point between the two C atoms. The electron-phonon matrix elements were interpolated from the coarse $4 \times 4 \times 4$ grid (for both phonons and electrons) to a $24 \times 24 \times 24$ grid for electrons, and directly on the phonon-dispersion path for phonons.

All calculations on the parent phase of $TmNiC_2$ were performed using the experimental structure at 400 K, while the q_{2c}-type CDW phase was derived theoretically in a supercell by following the soft eigenvector in the phonon dispersion of the parent phase, which is in excellent agreement with the experimental one.

III. RESULTS AND DISCUSSION

A. CDW and magnetic ordering

The starting point for our analysis is the careful and accurate determination of the boundaries between each magnetic phase, which leads to the construction of the $B - T$ phase diagram of $TmNiC_2$, with respect to a field applied along the crystallographic **a** axis, which is the easy direction of magnetization. As depicted in Fig. 2(a), the magnetic dome of $TmNiC_2$ contains three different types of magnetic orders, which are consistent with the preliminary diagram proposed by Kohsikawa *et al.* [43], which is complemented and further developed here. Apart from the high-temperature paramagnetic (PM) state (white background), one can distinguish the antiferromagnetic ground state (blue) as well as metamagnetic (yellow) and field-aligned ferromagnetic (red) states. The temperatures and magnetic fields corresponding to the transitions between the subsequent phases are obtained by means of bulk magnetic and thermal properties, respectively. The temperature dependencies of the magnetic susceptibility $\chi(T)$ and specific heat $C_p(T)$ show pronounced maxima at the Néel temperature T_N, as depicted in Fig. 2(b) and 2(d), while the field dependence of magnetization $M(B)$ [Fig. 2(c)] reveals the field-induced transitions to MM and FA-FM states manifesting as inflections at B_{c1} and B_{c2}, respectively. The precise position of these critical fields is determined from the maxima of the magnetization derivative with respect to the field, $\partial M/\partial B$. The field dependencies of all quantities have been corrected for the demagnetization factor: $B = \mu_0 H - NM$, where $\mu_0 H$ is the applied field and N relates to the sample shape [44]. Further details are included in the SM [35].

Figures 2(e) and 2(f) demonstrate the onset and development of q_2-type CDW, based on diffraction data obtained using laboratory diffractometer Bruker KAPPA APEX II. For further details on the experimental procedure and data refinement, see Ref. [31] and the SM [35]. The thermal dependence of the $q = (0.5, 3.5, 1.5)$ satellite reflection intensity is shown in Fig. 2(e), while Fig. 2(f) exhibits the temperature dependence of the Ni atoms' displacement δ from their positions along the **a** axis in the fundamental state (at $T > T_P$). Both $I_{sat}(T)$ and $\delta(T)$ saturate at lowest temperatures. Remarkably, the latter quantity, derived from single-crystal structure analysis, reaches a relatively large value of ≈ 0.21 Å, corresponding to $\approx 6\%$ of the average Ni-Ni distance. This observation is a characteristic landmark for the unconventional mechanisms [45,46] participating in CDW formation. In addition to the mechanism of Fermi surface nesting, the stronger electron-phonon coupling [47,48] seems to be involved in the stabilization of this state.

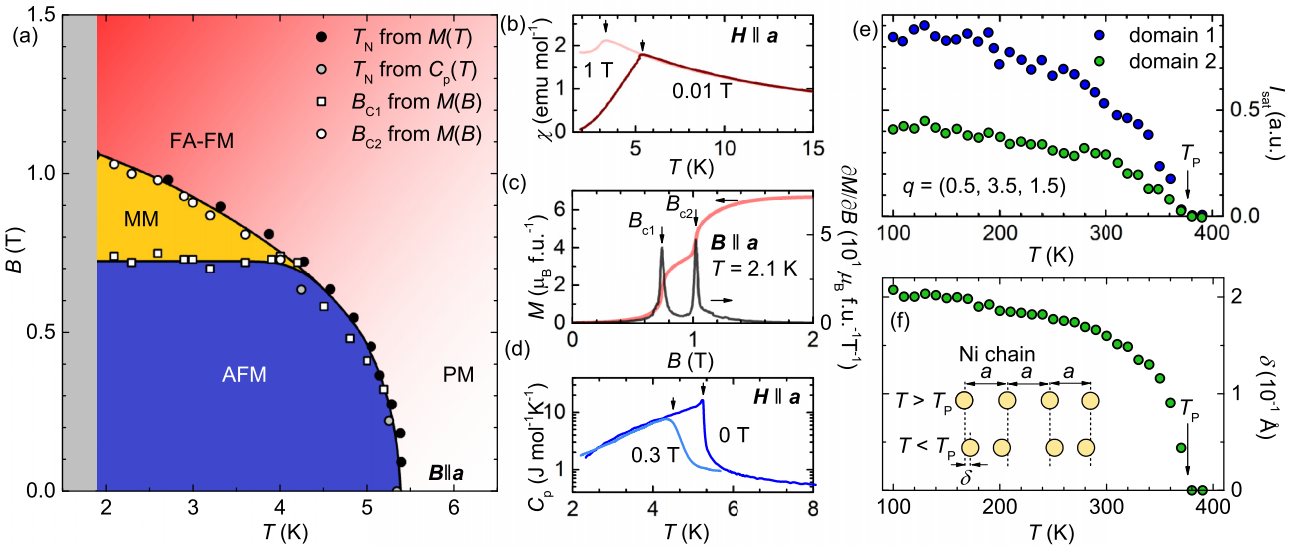

FIG. 2. Magnetism and CDW $TmNiC_2$. (a) Magnetic phase diagram including paramagnetic (PM), antiferromagnetic (AFM), field-induced metamagnetic (MM), and field-aligned ferromagnetic (FA-FM) states. Phase boundaries are constructed using the transition temperatures T_N and magnetic fields B_{c1} and B_{c2} obtained from temperature and field dependencies of the magnetization, as depicted in (b) and (c), as well as the temperature dependence of specific heat as shown in (d). Vertical arrows in (b)–(d) mark the transition temperatures and fields. (e) Thermal dependence of $q = (0.5,\ 3.5,\ 1.5)$ satellite peak intensity, corresponding to two crystallographic domains. Peierls temperature T_P as indicated by the onset of satellite intensity is marked using a vertical arrow. The presence of two twin domains, giving the same fundamental peaks but different sets of satellite reflections, is caused by twinning associated to the symmetry lowering from space group *Amm*2 (orthorhombic) to *Cm* (monoclinic) at the CDW transition [31]. (f) $\boldsymbol{a}$-axis direction displacement of the Ni atoms δ from the average position in the fundamental ($T > T_P$) state, as sketched in the inset.

B. Character of CDW transition

The strength of the electron-phonon mechanism relative to the Fermi surface nesting can be directly compared by means of density functional theory calculations [49,50]. In Fig. 3(a), we show the band structure of the parent and q_{2c}-type CDW phases following the same path in reciprocal space. In the parent phase, the bands cross the Fermi energy in the $S-R$, $Z-T$, $T-Y$, and $\Gamma-Z$ lines (for the full band structure in a wider energy range, we refer the reader to Fig. S7 of the SM [35]).

As shown in Fig. 3(a), the bands within the CDW phase exhibit the formation of 250 meV splittings near the Fermi level in the $S-R$, $T-Y$, and $\Gamma-Z$ lines. Together these lead to a pseudogap in the density of states (DOS). Going from the parent to the CDW phase, the DOS decreases from 0.605 to 0.408 states/(eV f.u. spin). The energy window in which the DOS of the CDW phase is lower than the parent phase, which we define as the CDW gap, is estimated to be 495 meV wide (see Fig. S8 of the SM [35]).

In Figs. 3(c) and 3(d), we show the Fermi surface (FS) of the parent (normal) state and within the q_{2c}-type CDW state, respectively. Both the unperturbed and distorted state FS show large similarities to those reported for $YNiC_2$ [51], and $LuNiC_2$ [52]. The main parts of the normal-state FS are quasiplanar sheets running perpendicularly to the $\mathbf{b}_3$ direction, with X-shaped valleys, as seen in the top view of Fig. 3(c). The Fermi surface also contains other characteristic features: hourglass-shaped columns connecting the sheets [highlighted with dashed black line rectangles in the top panel of Fig. 3(c)] and egg-shaped pockets. While the CDW transition removes the majority of the quasiplanar FS component, as demonstrated in Fig. 3(d), leaving only a sinelike sheet [highlighted with a solid black line bordered rectangle in the lower panel of Fig. 3(d)], the two smaller elements—columns and egg-shaped pockets—remain untouched. The Fermi surface decomposition into a set of partially connected or isolated pockets with dispersion in all three dimensions is consistent with the previously reported [31] loss of the transport properties' anisotropy upon lowering the temperature below $T_P = 375$ K.

To complement the electronic structure and its evolution, we proceed to discuss the vibrational properties and their interactions with the crystal lattice. In Fig. 4(a), we show the phonon dispersion for the normal phase of $TmNiC_2$. The phonon-dispersion branch exhibits two dips corresponding to the wave vectors $R = q_2 = (0.5, 0.5, 0.5)$ and $q_1 = (0.5, 0.56, 0)$, which is located between Z and A_0. The softening at q_2 is visibly stronger than the one at q_1, and the mode reaches an imaginary frequency at this point, being a hallmark of a phonon instability. The significantly weaker dip at q_1 suggests that the potential instability at this wave vector remains latent.

Armed with the details of electronic and phonon structures, we can directly examine the relative role of nesting and electron-phonon coupling strength by comparing the relevant quantities: nesting function $\chi_0(\mathbf{q})$, defined in the static limit as

$$\chi_0(\mathbf{q}) = \sum_{\mathbf{k}} \delta(\epsilon_{\mathbf{k}} - \epsilon_F)\delta(\epsilon_{\mathbf{k}+\mathbf{q}} - \epsilon_F), \tag{1}$$

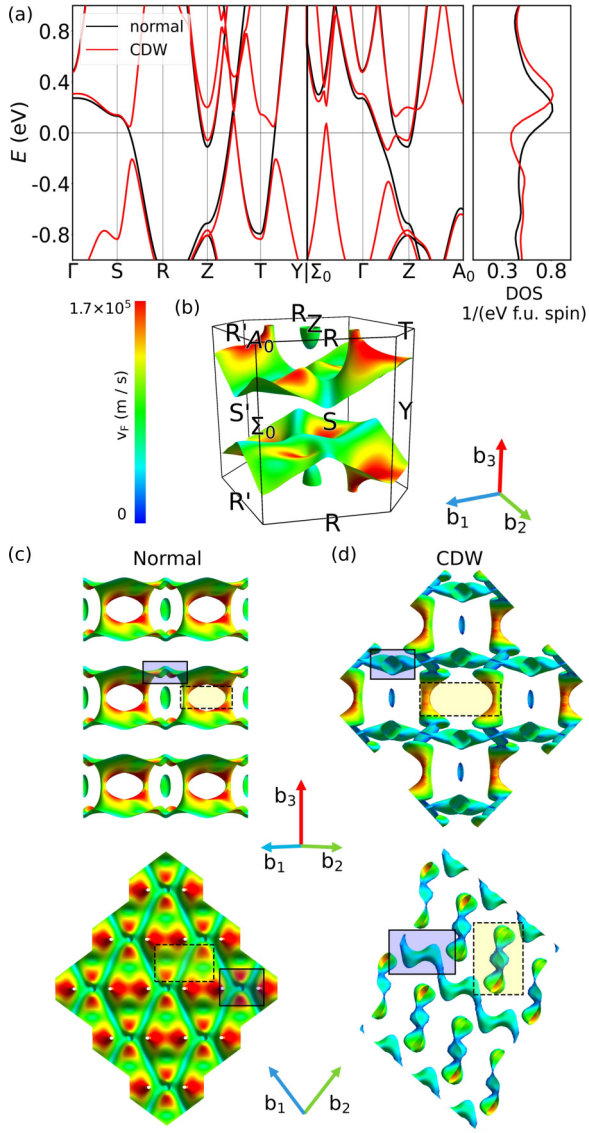

FIG. 3. (a) Electronic band structure and DOS of $TmNiC_2$ for both the normal phase (black line) and the q_{2c}-type CDW phase (red line). The Fermi energy is taken as zero. (b) The Fermi surface in the first Brillouin zone (FBZ) for the normal phase, along with the special points. (c) The Fermi surface for the normal phase from different perspectives (above, a lateral view; below, a top view). (d) Similarly, the Fermi surface for the q_{2c}-type CDW phase. The solid and dashed black boxes indicate the corresponding features in the Fermi surface of the two phases. The color scale represents the Fermi velocity. The high-symmetry $\mathbf{k}$ points in the FBZ are $\Gamma = (0, 0, 0)$, $S = (0, 0.5, 0)$, $R = (0, 0.5, 0.5)$, $Z = (0, 0, 0.5)$, $T = (-0.5, 0.5, 0.5)$, $Y = (-0.5, 0.5, 0)$, $\Sigma_0 = (0.39, 0.39, 0)$, and $A_0 = (0.39, 0.39, 0.5)$.

where ϵ_F is the Fermi energy while $\epsilon_{\mathbf{k}}$ and $\epsilon_{\mathbf{k}+\mathbf{q}}$ are the energies of the electronic states at the wave vectors $\mathbf{k}$ and $\mathbf{k}+\mathbf{q}$; and anisotropic electron-phonon coupling $\lambda_{\mathbf{q},\mu}$, with μ being the phonon mode. The nesting function and anisotropic coupling for the softest mode ($\mu = 1$) are shown in Fig. 4(b). For the two wave vectors corresponding to the soft modes (q_1 and q_2), we find peaks in both $\chi_0(\mathbf{q})$ and $\lambda_{\mathbf{q},\mu}$. However, the broadened and weak maxima of $\chi_0(\mathbf{q})$, similar to those of

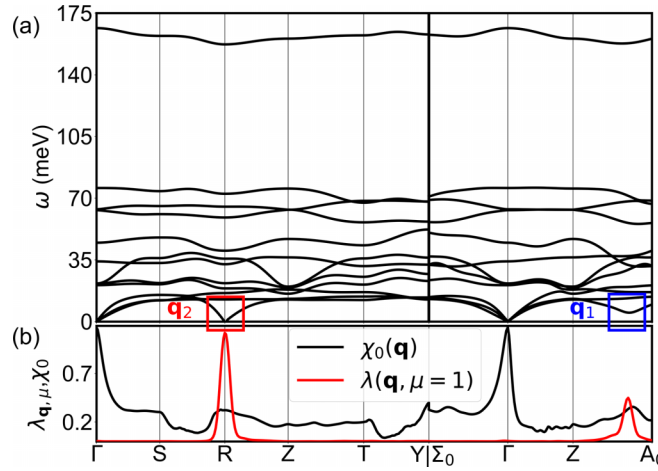

FIG. 4. (a) Phonon dispersion of $TmNiC_2$ revealing softening at the wave vectors q_2 and q_1, highlighted as a red and blue box, respectively. (b) Electron-phonon coupling $\lambda_{\mathbf{q},\mu}$ (red line) and nesting function χ_0 (black line).

$LaNiC_2$, which shows no CDW, contrast with the strong and well-defined peaks seen in the cases of $NdNiC_2$, $SmNiC_2$, and $GdNiC_2$ [53], indicating that nesting alone is not sufficient to drive the CDW transition in $TmNiC_2$. Moreover, the nesting function is also as large for other wave vectors (e.g., Y and Σ_0), for which we find no softening. In contrast to the weak and broadened peaks in $\chi_0(\mathbf{q})$, the electron-phonon coupling shows a sharp maximum at q_2, which corresponds to the observed CDW-related satellite peaks, and a smaller one at q_1. This result suggests that the electron-phonon coupling is the main mechanism for the CDW transition, which is consistent with the strong lattice distortion and the high intensity of satellite peaks. In other words, Fermi surface nesting has little predictive power and plays a lesser role compared to electron-phonon coupling.

C. Interplay between CDW and magnetism

Knowing that the momentum-dependent electron-phonon coupling plays a decisive role in CDW formation, we may now examine whether this mechanism can defend the CDW from being suppressed by long-range magnetism. To explore the interaction between charge density waves and phases present in the magnetic phase diagram of $TmNiC_2$ [see Fig. 2(a)], we performed synchrotron diffraction experiments at low temperatures ($T < 12$ K) and strong magnetic fields ($B \leqslant 3$ T), which allowed us to tune the magnetic state.

During the low-temperature diffraction experiment, we have selected and followed two satellite reflections, $q = (-0.5, 5.5, 7.5)$ and $q = (-0.5, 6.5, 8.5)$. Their nearest-neighbor fundamental Bragg peaks (0, 5, 7) and (0, 6, 8) have been used as the reference. Figures 5(a) and 5(b) depict the representative peak profiles, along k and h reciprocal lattice directions, measured at stable temperatures of $T = 11$ K (red) and 2.9 K (black), respectively. Within the experimental resolution, the reflections show the same shape intensity at both temperatures, standing above and below T_N, thus situated in PM and AFM phases, respectively. The zero-field thermal dependence of satellite peak

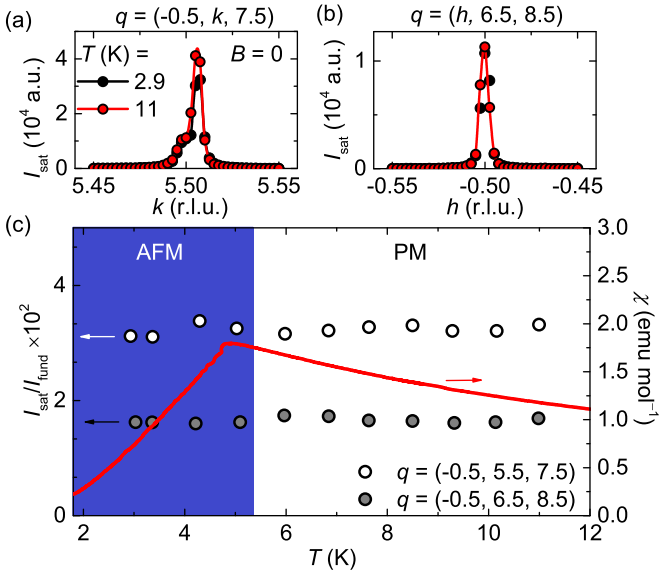

FIG. 5. CDW satellites across the antiferromagnetic transition. (a),(b) Reciprocal space profiles of (a) (−0.5, 5.5, 7.5) and (b) (−0.5, 6.5, 8.5) peaks at temperatures above and below T_N: at $T = 11$ K (red color) and $T = 2.9$ K (black), respectively. (c) Thermal dependence of these peaks' intensity normalized by the neighboring fundamental peaks (0, 5, 7) and (0, 6, 8), respectively (white and gray points respectively; left-hand scale) at the vicinity of T_N at zero applied field. The temperature dependence of magnetic susceptibility $\chi(T)$ measured at $\mu_0 H = 0.01$ T (red line; right-hand scale) illustrates the transition from a PM (white background) to AFM (blue background) state.

intensity normalized by the closest fundamental reflection is presented in Fig. 5(c), together with magnetic susceptibility, in which the pronounced maximum marks the magnetic transition. The courses of both $I_{sat}/I_{fund}(T)$ show a similar, flat shape, with no visible drop below T_N. This result stands in contrast with the behavior of the q_1-type CDW, which in $NdNiC_2$ and $GdNiC_2$ shows $\approx 50\%$ and $\approx 20\%$ intensity drop at the onset of the AFM state, respectively [19,20]. However, our observation reproduces the behavior reported for other $RNiC_2$ exhibiting CDW with the same q_2 type of modulation—namely, $DyNiC_2$, $HoNiC_2$, and $ErNiC_2$ [21], suggesting that robustness to the antiferromagnetic ground state is a common feature of these compounds. Confirming the coexistence of the q_2-type CDW with the antiferromagnetic ground state in $TmNiC_2$ opens a possibility and motivation to verify the hypothesis that CDW also coexists with the remaining ingredients of the magnetic phase diagram. With this aim, we have followed the same satellite reflections as a function of magnetic field applied along the **a** crystallographic axis [see a sketch in Fig. 6(a)] to subsequently scan from PM or AFM through the MM to FA-FM states. Figures 6(b) and 6(c) present the comparison of the reciprocal lattice profiles of the two explored satellite peaks, both measured at the lowest reached temperature of $T = 2.9$ K: at zero-field condition (black), corresponding to the AFM ground state, and at $B = 2.85$ T (red), situated deeply inside the FA-FM state region. Within the measurement resolution, no significant differences can be observed between the results obtained under these two conditions: the experiment reveals neither any substantial broadening or weakening of the satellite peaks' intensity, nor peak shifting. Furthermore, to exclude the structural changes at high fields and low temperatures, two $20^\circ\omega$ scans (rotation of the crystal about the **a** axis) with two 2θ positions of the detector were performed at 2 T and 2 K. Owing to the 5° x-ray window of the magnet (corresponding to more than a $h = -\frac{1}{2} \rightarrow \frac{1}{2}$ range) and the

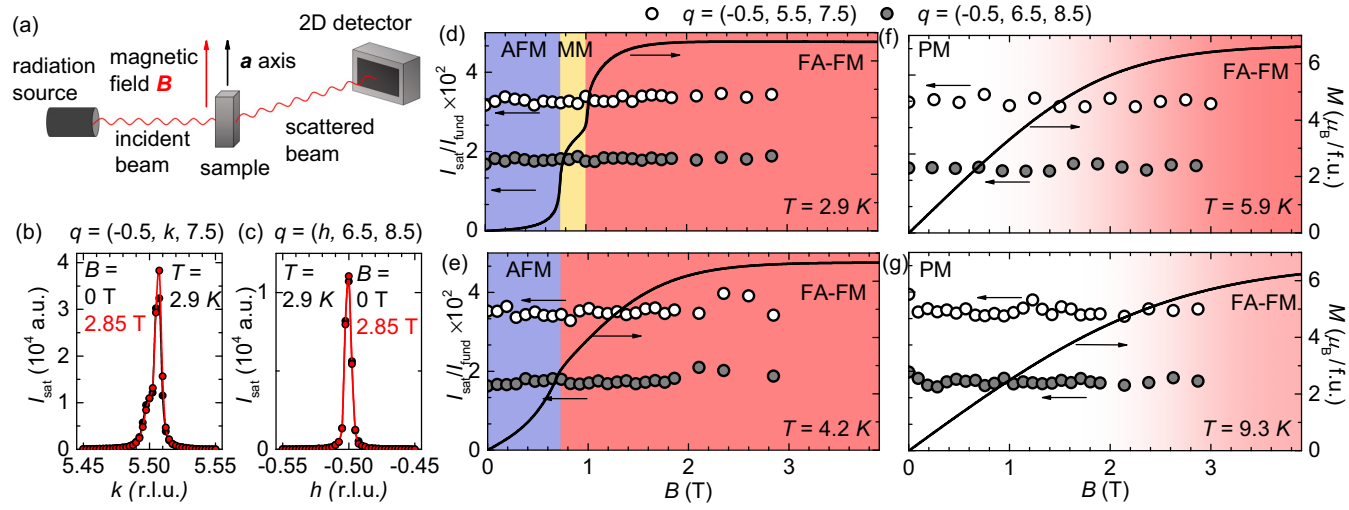

FIG. 6. CDW satellite peaks across the field-induced transitions. (a) Sketch of the synchrotron diffraction experiment geometry. Regardless of the scattering angle or detector position, the magnetic field (red arrow) is maintained along the ***a*** crystallographic axis (black arrow). (b),(c) Reciprocal space profiles of (b) (−0.5, 5.5, 7.5) and (c) (−0.5, 6.5, 8.5) peaks at zero field (black) and $B = 2.85$ T (red), respectively. (d)–(g) The field dependence of the intensity (white and gray points, respectively; left-hand scale) of the same peaks as in (b) and (c), normalized by the neighboring fundamental reflections [(0, 5, 7) and (0, 6, 8), respectively]. For clarity, the field dependence of magnetization is also plotted with a black line (right-hand scale). Labels and background colors indicate the relevant magnetic states: PM (white), AFM (blue), MM (yellow), and FA-FM (red) (see Fig. 1 for more details).

use of a two-dimensional (2D) detector, multiple Brillouin zones were thus recorded. Only the expected $h = 0$ main reflections and satellite $h = \pm\frac{1}{2}$ reflections were observed.

For a broader picture, in Figs. 6(c)–6(g), we have plotted the field dependence of the intensity of both satellites, normalized by the neighboring fundamental peaks $I_{sat}/I_{fund}(B)$, measured at various temperatures. The displayed course of magnetization $M(B)$ measured at the same temperature, as well as the background color, corresponding to the relevant regions of the diagram from Fig. 2(a), serve as a guide to assign the $B-T$ conditions to the underlying magnetic phases. Within the scan resolution, $I_{sat}/I_{fund}(B)$ for both measured satellites shows the same flat characteristics in the entire experimental range, with no drop or even a less pronounced downturn, regardless of the position in the magnetic phase diagram. Conservation of both the peak shape and its initial intensity indicates that both amplitude and spatial coherence length of the charge density wave, respectively, are preserved.

D. Discussion

This observation stands in even greater contrast to the response shown by the q_1-type CDW. Under similar circumstances—upon a transition to a FM ground state, as well as field-induced MM or FA-FM transitions—a q_1-type CDW suffers a rapid and complete obliteration [22–24]. Such a striking dissimilarity of the responses shown by these two CDW species suggests that the reason standing behind this observation is rooted at their origin. The conduction band's splitting, reaching the values at the order of the charge density wave gap [54] and consequent deterioration of Fermi nesting conditions, has been suggested to be the main mechanism causing the abrupt suppression of the q_1-type CDW at the onset of the FM ground state in $SmNiC_2$ [23]. The theoretical calculations performed for $LuNiC_2$ predict the q_2-CDW to open a partial gap at the order of $2\Delta_{CDW} \approx 300$ meV [52]. The same work estimates the maximum bands splitting due to the asymmetric spin-orbit coupling in this nonmagnetic sibling of $TmNiC_2$ at ≈ 74 meV, and a similar value of ≈ 84 meV has been calculated by Hase *et al.* [55] for $YNiC_2$. Although these models do not capture the ferromagnetic band's splitting amplification as expected in the FA-FM state of $TmNiC_2$, their results can serve as a useful guide. Even if greatly underestimated, the calculated magnitude of the band splitting remains a sizable fraction of the CDW band gap. Note that the saturation magnetization in the FA-FM state [see Figs. 2(c) and 6] is, in $TmNiC_2$, as high as in $GdNiC_2$ ($\approx 6\mu_B$/f.u. [56]) and an order of magnitude higher than in $SmNiC_2$ ($< 0.5\,\mu_B$/f.u. [57]). Therefore, one expects in $TmNiC_2$ at least the same or significantly stronger band splitting than in these compounds in which q_1-CDW is suppressed in the FA-FM and FM states, respectively. This comparison suggests that, similarly to the case of $SmNiC_2$, the Fermi surface geometry in $TmNiC_2$ is anticipated to be largely affected, yet, unexpectedly, the q_2-type CDW does not experience any, even weak, destructive consequences.

In order to become immune to the deterioration of nesting conditions and resulting CDW suppression, the q_2-type CDW must be stabilized by an additional factor. A mechanism that complements conventional Fermi surface nesting is associated with lattice degrees of freedom and is realized by the q-dependent electron-phonon coupling, which, if strong enough, can generate periodic lattice distortions. This is a way to stabilize the charge density wave [58–60] with a less decisive contribution from the electronic structure [49]. The important lattice component in $TmNiC_2$ is indicated by the pronounced transformation of the crystal structure at T_P, accompanied by symmetry descent and a significant anomaly of the specific heat [31]. This scenario is further supported by the large intensity of the satellite peaks and strong lattice distortion revealed by our high-temperature diffraction experiment.

Further arguments arise from our calculations of the electronic and phononic structures, which point to a major contribution of momentum-dependent electron-phonon coupling to the charge density wave transition. This result is in agreement with reports devoted to the characterization and the origin of the CDW states in $YNiC_2$ and $LuNiC_2$—nonmagnetic siblings of $TmNiC_2$. The conclusions raised by Steiner *et al.* [52], based on the calculated electronic structure of $LuNiC_2$, cast a shadow of doubt on nesting being solely responsible for the Peierls transition to a q_2-type CDW state. The analogous scenario is realized in $YNiC_2$, where the exploration of the electronic and phononic structures revealed that the decisive role in the stabilization of this state is played by the lattice degrees of freedom [51]. Thus, as anticipated, $TmNiC_2$, which in the $RNiC_2$ phase diagram is situated between heavier $LuNiC_2$ and lighter $YNiC_2$ [51,52], shares the main features of the electronic and phononic structures as well as the common roots of the q_2-type CDW state.

IV. CONCLUSIONS

In summary, we have performed a low-temperature and high magnetic field diffraction experiment to examine the charge density wave response through all the magnetic states comprised in the phase diagram of $TmNiC_2$. By following the CDW-related satellite reflections on the path from paramagnetic through antiferromagnetic and metamagnetic to field-aligned ferromagnetic states, and observing no signatures of even a weak erosion of their intensity, shape, or position, we directly demonstrate the evidence for the coexistence of a q_2-type CDW and all these types of long-range magnetism. We additionally confirm the robustness of a CDW-modulated state by reciprocal lattice scans, ruling out the appearance of additional superstructure reflections in any of the relevant magnetic phases. In striking contrast to the behavior of q_1-CDW in early lanthanide $RNiC_2$, the q_2-type CDW in $TmNiC_2$ remains unaffected even in the presence of aligned Ising-type magnetic moments with bulk magnetization as large as 7 μ_B/f.u. By DFT calculations, we also confirm the major contribution from momentum-dependent electron-phonon coupling into the CDW transition. A plausible explanation of the vastly divergent response to magnetic ordering by these two CDW types in the $RNiC_2$ family—the former being sensitive and the latter immune—to electronic band splitting, is their distinct foundation, with dominant inputs from Fermi surface nesting and coupling with the crystal lattice, respectively.

ACKNOWLEDGMENTS

The project is co-financed by a bilateral project of the Polish National Agency for Academic Exchange (NAWA) Grant No. PPN/BAT/2021/1/00016 and Austrian Academic Exchange Service ÖAD Grant No. PL04/2022. M.R. acknowledges the financial support by NAWA Grant No. BPN/BEK/2021/1/00245/DEC/1. S.D.C. acknowledges funding from the European Union - NextGenerationEU under the Italian Ministry of University and Research (MUR), "Network 4 Energy Sustainable Transition - NEST" Project (MIUR project code PE000021, Concession Degree No. 1561 of Oct. 11, 2022) No. CUP C93C22005230007. We acknowledge DESY (Hamburg, Germany), a member of the Helmholtz Association HGF, for the provision of experimental facilities. Parts of this research were carried out at the P09 beamline of PETRA III synchrotron. Beamline time was allocated for Proposal No. I-20230121 EC. The computational results presented here have been achieved using the Vienna Scientific Cluster (VSC).

[1] J. Chang, E. Blackburn, A. T. Holmes, N. B. Christensen, J. Larsen, J. Mesot, R. Liang, D. A. Bonn, W. N. Hardy, A. Watenphul, M. v. Zimmermann, E. M. Forgan, and S. M. Hayden, Direct observation of competition between superconductivity and charge density wave order in $YBa_2Cu_3O_{6.67}$, Nat. Phys. **8**, 871 (2012).

[2] X. F. Lu, N. Z. Wang, H. Wu, Y. P. Wu, D. Zhao, X. Z. Zeng, X. G. Luo, T. Wu, W. Bao, G. H. Zhang, F. Q. Huang, Q. Z. Huang, and X. H. Chen, Coexistence of superconductivity and antiferromagnetism in $(Li_{0.8}Fe_{0.2})$OHFeSe, Nat. Mater. **14**, 325 (2015).

[3] S. Kawasaki, Z. Li, M. Kitahashi, C. T. Lin, P. L. Kuhns, A. P. Reyes, and G. Q. Zheng, Charge-density-wave order takes over antiferromagnetism in $Bi_2Sr_{2-x}La_xCuO_6$ superconductors, Nat. Commun. **8**, 1267 (2017).

[4] Y. Song, T. Ying, X. Chen, X. Han, X. Wu, A. P. Schnyder, Y. Huang, J. G. Guo, and X. Chen, Competition of superconductivity and charge density wave in selective oxidized CsV_3Sb_5 thin flakes, Phys. Rev. Lett. **127**, 237001 (2021).

[5] L. Zeng, X. Hu, N. Wang, J. Sun, P. Yang, M. Boubeche, S. Luo, Y. He, J. Cheng, D.-X. Yao, and H. Luo, Interplay between charge-density-wave, superconductivity, and ferromagnetism in $CuIr_{2-x}Cr_xTe_4$ chalcogenides, J. Phys. Chem. Lett. **13**, 2442 (2022).

[6] X. Teng, J. S. Oh, H. Tan, L. Chen, J. Huang, B. Gao, J.-X. Yin, J.-H. Chu, M. Hashimoto, D. Lu, C. Jozwiak, A. Bostwick, E. Rotenberg, G. E. Granroth, B. Yan, R. J. Birgeneau, P. Dai, and M. Yi, Magnetism and charge density wave order in kagome FeGe, Nat. Phys. **19**, 814 (2023).

[7] M. A. Ruderman and C. Kittel, Indirect exchange coupling of nuclear magnetic moments by conduction electrons, Phys. Rev. **96**, 99 (1954).

[8] T. Kasuya, A theory of metallic ferro- and antiferromagnetism on Zener's model, Prog. Theor. Phys. **16**, 45 (1956).

[9] K. Yosida, Magnetic properties of Cu-Mn alloys, Phys. Rev. **106**, 893 (1957).

[10] R. E. Peierls, *Quantum Theory of Solids* (Oxford University Press, Oxford, 1955).

[11] H. Fröhlich, On the theory of superconductivity: The one-dimensional case, Proc. R. Soc. London A **223**, 296 (1954).

[12] T. Kurumaji, T. Nakajima, M. Hirschberger, A. Kikkawa, Y. Yamasaki, H. Sagayama, H. Nakao, Y. Taguchi, T.-H. Arima, and Y. Tokura, Skyrmion lattice with a giant topological Hall effect in a frustrated triangular-lattice magnet, Science **365**, 914 (2019).

[13] D. S. Inosov, D. V. Evtushinsky, A. Koitzsch, V. B. Zabolotnyy, S. V. Borisenko, A. A. Kordyuk, M. Frontzek, M. Loewenhaupt, W. Löser, I. Mazilu, H. Bitterlich, G. Behr, J.-U. Hoffmann, R. Follath, and B. Büchner, Electronic structure and nesting-driven enhancement of the RKKY interaction at the magnetic ordering propagation vector in Gd_2PdSi_3 and Tb_2PdSi_3, Phys. Rev. Lett. **102**, 046401 (2009).

[14] T. H. Salters, F. Orlandi, T. Berry, J. F. Khoury, E. Whittaker, P. Manuel, and L. M. Schoop, Charge density wave-templated spin cycloid in topological semimetal $NdSb_xTe_{2-x-\delta}$, Phys. Rev. Mater. **7**, 044203 (2023).

[15] P. M. Coelho, K. Nguyen Cong, M. Bonilla, S. Kolekar, M.-H. Phan, J. Avila, M. C. Asensio, I. I. Oleynik, and M. Batzill, Charge density wave state suppresses ferromagnetic ordering in VSe_2 monolayers, J. Phys. Chem. C **123**, 14089 (2019).

[16] S. Ramakrishnan, A. Schönleber, T. Rekis, N. van Well, L. Noohinejad, S. van Smaalen, M. Tolkiehn, C. Paulmann, B. Bag, A. Thamizhavel, D. Pal, and S. Ramakrishnan, Unusual charge density wave transition and absence of magnetic ordering in $Er_2Ir_3Si_5$, Phys. Rev. B **101**, 060101(R) (2020).

[17] J. Zhou, Z. Wang, S. Wang, Y. P. Feng, M. Yang, and L. Shen, Coexistence of ferromagnetism and charge density waves in monolayer $LaBr_2$, Nanoscale Horiz. **8**, 1054 (2023).

[18] A. Wölfel, L. Li, S. Shimomura, H. Onodera, and S. van Smaalen, Commensurate charge-density wave with frustrated interchain coupling in $SmNiC_2$, Phys. Rev. B **82**, 054120 (2010).

[19] N. Yamamoto, R. Kondo, H. Maeda, and Y. Nogami, Interplay of charge-density wave and magnetic order in ternary rare-earth nickel carbides, $RNiC_2$ (R = Pr and Nd), J. Phys. Soc. Jpn. **82**, 123701 (2013).

[20] S. Shimomura, C. Hayashi, N. Hanasaki, K. Ohnuma, Y. Kobayashi, H. Nakao, M. Mizumaki, and H. Onodera, Multiple charge density wave transitions in the antiferromagnets $RNiC_2$ (R = Gd, Tb), Phys. Rev. B **93**, 165108 (2016).

[21] H. Maeda, R. Kondo, and Y. Nogami, Multiple charge density waves compete in ternary rare-earth nickel carbides, $RNiC_2$ (R: Y, Dy, Ho, and Er), Phys. Rev. B **100**, 104107 (2019).

[22] N. Hanasaki, S. Shimomura, K. Mikami, Y. Nogami, H. Nakao, and H. Onodera, Interplay between charge density wave and antiferromagnetic order in $GdNiC_2$, Phys. Rev. B **95**, 085103 (2017).

[23] S. Shimomura, C. Hayashi, G. Asaka, N. Wakabayashi, M. Mizumaki, and H. Onodera, Charge-Density-Wave Destruction and Ferromagnetic Order in $SmNiC_2$, Phys. Rev. Lett. **102**, 076404 (2009).

[24] N. Hanasaki, Y. Nogami, M. Kakinuma, S. Shimomura, M. Kosaka, and H. Onodera, Magnetic field switching of the charge-density-wave state in the lanthanide intermetallic $SmNiC_2$, Phys. Rev. B **85**, 092402 (2012).

[25] K. K. Kolincio, M. Roman, and T. Klimczuk, Enhanced mobility and large linear nonsaturating magnetoresistance in the magnetically ordered states of $TmNiC_2$, Phys. Rev. Lett. **125**, 176601 (2020).

[26] K. K. Kolincio, M. Roman, F. Garmroudi, M. Parzer, E. Bauer, and H. Michor, Charge density wave, enhanced mobility, and large nonsaturating magnetoresistance across the magnetic states of $HoNiC_2$ and $ErNiC_2$, Phys. Rev. B **109**, 075154 (2024).

[27] R. Ray, B. Sadhukhan, M. Richter, J. I. Facio, and J. van den Brink, Tunable chirality of noncentrosymmetric magnetic Weyl semimetals in rare-earth carbides, npj Quantum Mater. **7**, 19 (2022).

[28] G. Grüner, The dynamics of charge-density waves, Rev. Mod. Phys. **60**, 1129 (1988).

[29] P. Monceau, Electronic crystals: An experimental overview, Adv. Phys. **61**, 325 (2012).

[30] J. Chang, E. Blackburn, O. Ivashko, A. T. Holmes, N. B. Christensen, M. Hücker, R. Liang, D. A. Bonn, W. N. Hardy, U. Rütt, M. v. Zimmermann, E. M. Forgan, and S. M. Hayden, Magnetic field controlled charge density wave coupling in underdoped $YBa_2Cu_3O_{6+x}$, Nat. Commun. **7**, 11494 (2016).

[31] M. Roman, M. Fritthum, B. Stöger, D. T. Adroja, and H. Michor, Charge density wave and crystalline electric field effects in $TmNiC_2$, Phys. Rev. B **107**, 125137 (2023).

[32] Bruker, *APEXII, SAINT and SADABS* (Bruker Analytical X-ray Instruments, Inc., Madison, WI, 2023).

[33] J. Strempfer, S. Francoual, D. Reuther, D. K. Shukla, A. Skaugen, H. Schulte-Schrepping, T. Kracht, and H. Franz, Resonant scattering and diffraction beamline P09 at PETRA III, J. Synchrotron Radiat. **20**, 541 (2013).

[34] S. Francoual, J. Strempfer, J. Warren, Y. Liu, A. Skaugen, S. Poli, J. Blume, F. Wolff-Fabris, P. C. Canfield, and T. Lograsso, Single-crystal X-ray diffraction and resonant x-ray magnetic scattering at helium-3 temperatures in high magnetic fields at beamline P09 at PETRA III, J. Synchrotron Radiat. **22**, 1207 (2015).

[35] See Supplemental Material at http://link.aps.org/supplemental/10.1103/PhysRevB.111.245116 for further details and descriptions of the used methods, details of the temperature rise estimate, and complementary data, which includes Refs. [61–66].

[36] P. Giannozzi, S. Baroni, N. Bonini, M. Calandra, R. Car, C. Cavazzoni, D. Ceresoli, G. L. Chiarotti, M. Cococcioni, I. Dabo, A. Dal Corso, S. de Gironcoli, S. Fabris, G. Fratesi, R. Gebauer, U. Gerstmann, C. Gougoussis, A. Kokalj, M. Lazzeri, L. Martin-Samos *et al.*, Quantum Espresso: A modular and open-source software project for quantum simulations of materials, J. Phys.: Condens. Matter **21**, 395502 (2009).

[37] P. Giannozzi, O. Andreussi, T. Brumme, O. Bunau, M. B. Nardelli, M. Calandra, R. Car, C. Cavazzoni, D. Ceresoli, M. Cococcioni *et al.*, Advanced capabilities for materials modelling with QUANTUM ESPRESSO, J. Phys.: Condens. Matter **29**, 465901 (2017).

[38] J. Noffsinger, F. Giustino, B. D. Malone, C.-H. Park, S. G. Louie, and M. L. Cohen, EPW: A program for calculating the electron-phonon coupling using maximally localized Wannier functions, Comput. Phys. Commun. **181**, 2140 (2010).

[39] S. Poncé, E. R. Margine, C. Verdi, and F. Giustino, Epw: Electron-phonon coupling, transport and superconducting properties using maximally localized Wannier functions, Comput. Phys. Commun. **209**, 116 (2016).

[40] H. Lee, S. Poncé, K. Bushick, S. Hajinazar, J. Lafuente-Bartolome, J. Leveillee, C. Lian, J.-M. Lihm, F. Macheda, H. Mori *et al.*, Electron-phonon physics from first principles using the EPW code, npj Comput. Mater. **9**, 156 (2023).

[41] D. R. Hamann, Optimized norm-conserving Vanderbilt pseudopotentials, Phys. Rev. B **88**, 085117 (2013).

[42] J. P. Perdew, K. Burke, and M. Ernzerhof, Generalized gradient approximation made simple, Phys. Rev. Lett. **77**, 3865 (1996).

[43] Y. Koshikawa, H. Onodera, M. Kosaka, H. Yamauchi, M. Ohashi, and Y. Yamaguchi, Crystalline electric fields and magnetic properties of single-crystalline $RNiC_2$ compounds (R = Ho, Er and Tm), J. Magn. Magn. Mater. **173**, 72 (1997).

[44] A. Aharoni, Demagnetizing factors for rectangular ferromagnetic prisms, J. Appl. Phys. **83**, 3432 (1998).

[45] W. L. McMillan, Landau theory of charge-density waves in transition-metal dichalcogenides, Phys. Rev. B **12**, 1187 (1975).

[46] R. H. Friend and D. Jerome, Periodic lattice distortions and charge density waves in one- and two-dimensional metals, J. Phys. C **12**, 1441 (1979).

[47] C. M. Varma and A. L. Simons, Strong-coupling theory of charge-density-wave transitions, Phys. Rev. Lett. **51**, 138 (1983).

[48] F. Galli, R. Feyerherm, R. W. A. Hendrikx, E. Dudzik, G. J. Nieuwenhuys, S. Ramakrishnan, S. D. Brown, S. van Smaalen, and J. A. Mydosh, Coexistence of charge density wave and antiferromagnetism in $Er_5Ir_4Si_{10}$, J. Phys.: Condens. Matter **14**, 5067 (2002).

[49] M. D. Johannes and I. I. Mazin, Fermi surface nesting and the origin of charge density waves in metals, Phys. Rev. B **77**, 165135 (2008).

[50] C.-S. Lian, C. Heil, X. Liu, C. Si, F. Giustino, and W. Duan, Coexistence of superconductivity with enhanced charge density wave order in the two-dimensional limit of $TaSe_2$, J. Phys. Chem. Lett. **10**, 4076 (2019).

[51] M. Roman, S. D. Cataldo, B. Stöger, L. Reisinger, E. Morineau, K. K. Kolincio, and H. Michor, Competing charge density wave phases in $YNiC_2$, Phys. Rev. B **111**, 195101 (2025).

[52] S. Steiner, H. Michor, O. Sologub, B. Hinterleitner, F. Höfenstock, M. Waas, E. Bauer, B. Stöger, V. Babizhetskyy, V. Levytskyy, and B. Kotur, Single-crystal study of the charge density wave metal $LuNiC_2$, Phys. Rev. B **97**, 205115 (2018).

[53] J. Laverock, T. D. Haynes, C. Utfeld, and S. B. Dugdale, Electronic structure of $RNiC_2$ (R = Sm, Gd, and Nd) intermetallic compounds, Phys. Rev. B **80**, 125111 (2009).

[54] J. N. Kim, C. Lee, and J.-H. Shim, Chemical and hydrostatic pressure effect on charge density waves of $SmNiC_2$, New J. Phys. **15**, 123018 (2013).

[55] I. Hase and T. Yanagisawa, Electronic structure of $RNiC_2$ (R = La, Y, and Th), J. Phys. Soc. Jpn. **78**, 084724 (2009).

[56] N. Hanasaki, K. Mikami, S. Torigoe, Y. Nogami, S. Shimomura, M. Kosaka, and H. Onodera, Successive transition in rare-earth intermetallic compound $GdNiC_2$, J. Phys.: Conf. Ser. **320**, 012072 (2011).

[57] H. Onodera, Y. Koshikawa, M. Kosaka, M. Ohashi, H. Yamauchi, and Y. Yamaguchi, Magnetic properties of single-crystalline RNiC$_2$ compounds (R = Ce, Pr, Nd and Sm), J. Magn. Magn. Mater. **182**, 161 (1998).

[58] H.-M. Eiter, M. Lavagnini, R. Hackl, E. A. Nowadnick, A. F. Kemper, T. P. Devereaux, J.-H. Chu, J. G. Analytis, I. R. Fisher, and L. Degiorgi, Alternative route to charge density wave formation in multiband systems, Proc. Natl. Acad. Sci. **110**, 64 (2013).

[59] X. Zhu, Y. Cao, J. Zhang, E. W. Plummer, and J. Guo, Classification of charge density waves based on their nature, Proc. Natl. Acad. Sci. **112**, 2367 (2015).

[60] J. Z. Xuetao Zhu, Jiandong Guo and E. W. Plummer, Misconceptions associated with the origin of charge density waves, Adv. Phys.: X **2**, 622 (2017).

[61] S. Kriminski, M. Kazmierczak, and R. E. Thorne, Heat transfer from protein crystals: Implications for flash-cooling and x-ray beam heating, Acta Crystallogr. Sect. D **59**, 697 (2003).

[62] A. Mhaisekar, M. J. Kazmierczak, and R. Banerjee, Three-dimensional numerical analysis of convection and conduction cooling of spherical biocrystals with localized heating from synchrotron x-ray beams, J. Synchrotron Radiat. **12**, 318 (2005).

[63] M. J. Berger, J. H. Hubbell, S. M. Seltzer, J. Chang, J. S. Coursey, R. Sukumar, D. S. Zucker, and K. Olsen, *Xcom: Photon Cross Section Database (Ver. 1.2)* (National Institute of Standards and Technology, Gaithersburg, MD, 1998).

[64] J. H. Kim, J.-S. Rhyee, and Y. S. Kwon, Magnon gap formation and charge density wave effect on thermoelectric properties in the SmNiC$_2$ compound, Phys. Rev. B **86**, 235101 (2012).

[65] B. Daudin, W. Mutscheller, and M. Wagner, Heat conductivity of the cooperative vibronic system TmVO$_4$, Physica Status Solidi (B) **122**, 73 (1984).

[66] P. J. Ellis and H. J. Bernstein, CBFlib (2015), http://www.bernstein-plus-sons.com/software/CBF/doc/CBFlib.html.